Modeling the effects of defect parameters on the performance of a p-$BaSi_2$/n-Si heterojunction solar cell

Tianguo Deng[a], Zhihao Xu[a], Yudai Yamashita[a], Takuma Sato[a], Kaoru Toko[a], Takashi Suemasu[a*]

[a] *Institute of Applied Physics, University of Tsukuba, Tsukuba, Ibaraki 305-8573, Japan*

* Corresponding author.

Electronic mail: suemasu@bk.tsukuba.ac.jp

Key words:

barium disilicide; solar cell; defect; simulation.

Abstract

Barium disilicide ($BaSi_2$) in thin-film solar cell applications has drawn considerable interest owing to its promising optical and electrical properties. We have achieved an efficiency of 9.9% in p-$BaSi_2$/n-Si heterojunction solar cells, which is the highest performance reported among semiconducting silicide devices; however, this value remains much lower than the theoretical limit as defined by the material's band gap. In this paper, we performed numerical simulations based on Silvaco ATLAS to investigate the effects of defect parameters on the performance of heterojunction solar cells. The defects were modeled by introducing two tail bands around the edge of the conduction and valence bands, and an acceptor-like Gaussian distributed localized energy level within the band gap of $BaSi_2$. The influence of the band tail density of states and the parameters of the localized energy levels on the short-circuit current density, open-circuit voltage, fill factor, and efficiency were evaluated. These results enabled us to reproduce the measured *J-V* characteristics by simulation.

Graphical abstract

We propose a defect model of p-$BaSi_2$ films to reproduce experimentally obtained current-voltage characteristics of p-$BaSi_2$/n-Si heterojunction solar cell under AM1.5 illumination. Two band tails and one acceptor-like localized energy level reproduces the experimental result.

1. Introduction

Thin-film solar cell materials such as CdTe, CIGS, and organic-inorganic perovskites, have drawn interest for achieving high energy conversion efficiencies η at low-cost [1-4]. However, many of these materials contain rare and/or toxic elements. Hence, there is a need to explore thin-film solar cell materials that are environmentally friendly. Si thin-film solar cells have also been studies; however, it is difficult to achieve η higher than 20% [5-10]. Among many candidate materials, we have focused on semiconducting barium disilicide $BaSi_2$, owing to its safe, stable, and abundant constituent elements [11]. $BaSi_2$ films can be grown by general techniques such as magnetron sputtering, vacuum evaporation, and molecular beam epitaxy [12-15]. $BaSi_2$ has a suitable band gap E_g of 1.3 eV [16,17], which matches the solar spectrum, and a high optical absorption coefficient α of 3×10^4 cm^{-1} at 1.5 eV [17,18], which is nearly 40 times as great as that of crystalline silicon. This means that short-wavelength photons are absorbed in the region close to defective surfaces. Therefore, surface passivation is very important to improve η [19]. Moreover, a long minority-carrier lifetime τ of approximately 10 μs [20,21] results in a minority-carrier diffusion length L of approximately 10 μm [22], which is much larger than the grain size of $BaSi_2$ because of inactive grain boundaries [23]. One unique feature of $BaSi_2$ is that large values of τ and L can be achieved simultaneously, indicating the great potential of $BaSi_2$ as a light absorbing layer for thin-film solar cell applications [24]. Several $BaSi_2$-based solar cells have been proposed, including $BaSi_2$ nanowires, back-contacted $BaSi_2$, and perovskite/$BaSi_2$ dual-junction solar cells [25-27]. The carrier conductivity type and concentration can be effectively controlled by impurity doping. In particular, the electron and hole concentrations can be controlled over a wide range between 10^{16} and 10^{20} cm^{-3} by Sb and B doping, respectively [5,28,29]. Such high electron and hole concentrations ensure that the material can operate as both electron and hole transport layers in a homojunction solar cell. Numerical simulation and optimization of Si/$BaSi_2$ heterojunction and $BaSi_2$ homojunction solar cells have also been reported [30].

Recently, the operation of a $BaSi_2$ homojunction solar cell has been reported for the first time, showing that the photogenerated carriers in the $BaSi_2$ layer can be separated by the built-in electric field in a homojunction diode [31,32].

The value of η in p-$BaSi_2$/n-Si heterojunction solar cells has approached 10% without any special passivation treatment formed on both Si(111) and Si(001) substrates [33-35]. This value is the highest reported for solar cells fabricated with semiconducting silicides; however, η remains lower than the theoretical limit as defined by its band gap [36]. Deep level transient spectroscopy revealed that undoped n-$BaSi_2$ films contain a hole trap level with a density of 1×10^{13} cm^{-3} at 0.27 eV from the valence band maximum (VBM) [37]. Electron paramagnetic resonance was also found to be an effective means to detect defects in $BaSi_2$ which carry a charge and have a spin [38]. However, there is almost the lack of information on defects in B-doped p-$BaSi_2$. In this work, we performed numerical simulation with the use of Silvaco ATLAS software to model the aforementioned solar cell and clarify the effects of different defect characteristics present in $BaSi_2$ on the p-$BaSi_2$/n-Si heterojunction solar cell performance.

2. Model

Silvaco ATLAS software, a physically-based two- and three-dimensional device simulator, treats solar cell performance according to Poisson's equation, the continuity equations of electrons and holes, and transport equations through a defined grid, helping us to understand and depict the physical processes of specified semiconductor structures associated with device operation and make reliable predictions about device behavior [39-43].

The structure and corresponding mesh of the p-$BaSi_2$/n-Si heterojunction solar cell is shown in Fig. 1(a). A non-uniform mesh, where the grid is finer around the interface, was defined to obtain good accuracy with a reasonable calculation time. Notably, the $BaSi_2$ film acts as an emitter of the p-n junction and a light absorbing layer. Figure 1(b) shows schematic

band diagrams of the heterojunction in thermodynamic equilibrium. The conduction-band offset ΔE_C and valence-band offset ΔE_V, owing to the difference in the electron affinity of $BaSi_2$ [44] and Si, promote separation of photogenerated carriers in p-$BaSi_2$ and those in n-Si to ensure good carrier collection.

The accuracy of the material parameters defined in the solar cell model, such as E_g, electron and hole concentrations (n and p) and carrier mobility (μ_e and μ_h) [45], permittivity, affinity, carrier lifetime (τ_e and τ_h), and the effective density of states in the conduction and valence bands (N_C and N_V) [46], determine the accuracy of the simulation results. Shockley–Read–Hall (SRH) recombination, which is the main recombination mechanism in $BaSi_2$ [21], is associated with the Fermi–Dirac statistics and was also considered. We used the experimentally determined carrier mobility [45] and carrier lifetime of $BaSi_2$ [20,47]. The input parameters for the simulation are given in Table 1 [11]. One of the most important sets of parameters for advanced solar cell modeling is the optical properties containing the refractive index n' and extinction coefficient κ versus wavelength λ, which decide the transmission and attenuation of light passing through the semiconductor, respectively. The n' and κ values of $BaSi_2$ were extracted from experimental results [17,27], where κ was calculated from the relationship $\alpha = 4\pi\kappa/\lambda$. Figure 2 shows the absorption coefficient of $BaSi_2$ and other solar cell materials [27,48-50]. The absorption spectrum of $BaSi_2$ is similar to that of other thin-film solar cell materials, such as CdTe, CIGS, and $CH_3NH_3PbI_3$ in the ultraviolet and visible regions. Notably, α of $BaSi_2$ is higher than those of CdTe and $CH_3NH_3PbI_3$ in the near-infrared region. This comparison demonstrates the excellent optical properties of $BaSi_2$.

The simulated current density versus voltage (J-V) characteristics under AM1.5 illumination for an idealized p-$BaSi_2$/n-Si heterojunction solar cell are compared with measurements of a real device in Fig. 3(a). The simulated short-circuit current density (J_{SC}) of 39.0 mA/cm^2, open-circuit voltage (V_{OC}) of 0.63 V and η of 15.7% were greater than those of a measured device, which had J_{SC}, V_{OC}, and η being 35.8 mA/cm^2, 0.47 V, and 9.9%,

respectively [34]. The major difference between these devices is that the simulated device is assumed to be free of defects. The simulation results should match those of the real device; otherwise, the results are not useful for designing and improving real devices. Therefore, to reproduce the measured *J-V* characteristics, we introduced defects into the simulated p-$BaSi_2$ film. In the p-$BaSi_2$ film, we assumed three components for the density of states (DOS): two band tails exponentially decayed from the conduction band minimum (CBM) and the VBM, one acceptor-like localized energy level characterized by a Gaussian distribution, which created a continuous distribution of trapping centers in the band gap of p-$BaSi_2$ [51]. The total density of states within the band gap $g(E)$ is given by [39]:

$$g(E) = G_{\mathrm{TA}} exp\left(\frac{E_{\mathrm{V}} - E}{E_{\mathrm{U}}}\right) + G_{\mathrm{TD}} exp\left(\frac{E - E_{\mathrm{C}}}{E_{\mathrm{U}}}\right) + G_{\mathrm{GA}} exp\left[-\frac{1}{2}\left(\frac{E_{\mathrm{GA}} - E}{W_{\mathrm{GA}}}\right)^2\right], \quad (1)$$

where E_{C} (E_{V}) is the CBM (VBM), G_{TA} (G_{TD}) is the effective density of acceptor (donor)-like tail states, E_{U} is the Urbach tail energy [52], G_{GA} is the effective density of acceptor-like states in a Gaussian distribution, E_{GA} is the peak energy of the Gaussian distribution of acceptor-like states, and W_{GA} is the standard deviation of the Gaussian distribution of acceptor-like states. The energies E_{U} and W_{GA} express to what extent those defective states distribute in the energy range. The capture cross-sections for majority carrier (hole) and minority carrier (electron) are set to be 1×10^{-14} and 1×10^{-16} cm^2, respectively for all states [40]. A schematic representation of such states is shown in Fig. 3(b) with the parameters of the band tails and localized energy level summarized in Table 2. Regarding the Urbach tail energy we fitted the measured absorption spectrum of p-type $BaSi_2$ films using the empirical rule expressed by [52],

$$\alpha(\hbar\omega) = \alpha_0 exp\left(\frac{\hbar\omega - E_g}{E_{\mathrm{U}}}\right), \quad (2)$$

where α_0 is constant and $\hbar\omega$ is the photon energy. E_{U} is an inverse logarithmic slope of the Urbach tail, and was found to be approximately 0.10 eV. That's why we set E_{U} at 0.10 eV in Table 2. Please note that the series resistance R_{S} and the shunt resistance R_{SH} are not the input

parameters in the simulation even though they can be obtained experimentally by the inverse of the slope of the measured *J-V* characteristics at around an open-circuit voltage and 0 V, respectively. They were determined by changing the parameters in Eq. (1) so that the simulation result reproduced the measured *J-V* characteristics. We also neglected the contact resistance at the ITO/p-$BaSi_2$ and Al/n-Si interfaces. This is because they were too small to explain the measured R_S. Regarding R_{SH}, ideally, it should be infinitely high. The presence of R_{SH} means the presence of leakage current. This is caused by recombination of photogenerated carriers via defect levels. They are also determined by parameters in Eq. (1).

3. Results and discussion

From the introduced defect model, we first investigated the effects of the defect parameters G_{TA}(G_{TD}), E_U, G_{GA}, E_{GA}, and W_{GA} on solar cell performance. We considered the effects of the above-mentioned parameters individually, while maintaining other parameters constant, as defined in Table 2. The localized defect level located at 0.37 eV above the valence band edge can be linked to acceptor-like impurities, such as dangling bonds in the Si tetrahedra of the $BaSi_2$ lattice, neutral non-ionized boron or oxygen atoms [51,53,54].

3.1 Urbach tail energy

Although the Urbach tail energy E_U was obtained to be 0.10 eV, we varied it symmetrically from 0.02 to 0.20 eV for the CBM and VBM to see its influence on the *J-V* characteristics. The *J-V* curves of the simulated solar cell versus E_U are shown in Fig. 4. The V_{OC} does not change with E_U, meaning that E_U does not have a major effect on the solar cell performance.

3.2 Density of states of band tails

We next discuss the effect of band tail density of states G_{TA} (G_{TD}) on the solar cell

performance. Here, the conduction and valence band tails are considered to be symmetric, that is $G_{TA}(E) = G_{TD}(E_C - E)$, and was varied from 1×10^{13} to 1×10^{23} $cm^{-3}\,eV^{-1}$. At the same time, the DOS of the acceptor-like localized energy level was maintained at $G_{GA} = 1 \times 10^{15}$ $cm^{-3}\,eV^{-1}$ and hence has a negligible effect on the solar cell performance. The simulated *J-V* curves are shown in Fig. 5(a). Figure 5(b) shows the J_{SC}, V_{OC}, *FF*, and η as a function of G_{TA} (G_{TD}), as extracted from the *J-V* curves. These four parameters remained unchanged with G_{TA} (G_{TD}) up to 1×10^{20} $cm^{-3}\,eV^{-1}$. When G_{TA} (G_{TD}) > 10^{20} $cm^{-3}eV^{-1}$, the solar cell performance started to degrade. The degradation of the J_{SC} can be explained by the fact that the photogenerated carriers are captured by the more densely distributed defects. Simultaneously, the values of *FF* and η markedly decreased and the shape of the *J-V* curves takes on an *S*-shape, indicating the presence of a barrier at the p-$BaSi_2$/n-Si interface. This result demonstrates that defects may act as dopants, which modify the doping profile and reduce the depletion region around the junction. The main difference between the ideal and measured p-$BaSi_2$/n-Si heterojunction solar cells is the magnitude of V_{OC}, in that the simulated *J-V* curves do not match those measured for the device by changing only E_U and G_{TA} (G_{TD}).

3.3 Standard deviation of the Gaussian distribution of localized energy level

W_{GA} corresponds to the defect dispersion, which shows the energy range where the localized energy levels are located within the band gap. The simulated *J-V* curves are shown in Fig. 6(a). Here, W_{GA} ranged from 0.04 to 0.57 eV and G_{GA} was maintained at 1×10^{15} cm^{-3} eV^{-1}. When the value of W_{GA} increased, J_{SC} and V_{OC} remained unchanged. We speculate that this result can be attributed to G_{GA} and E_{GA} being set at constant values. However, the values of *FF* and η decreased markedly when W_{GA} was larger than 0.2 eV. Figure 6(b) shows the response of *FF* and η to W_{GA}. The decrease of *FF* with increasing W_{GA} can be explained by the increase of R_S modeling the resistive losses of materials and the decrease of R_{SH} representing an increase of the parasitic leakage current that crosses the cell. The increase of

W_{GA} enhances the recombination of photogenerated carriers via defect levels, resulting in a decrease of R_{SH}. Lock-in thermography used for crystalline Si solar cells may also give us information about leakage currents in $BaSi_2$ solar cells [55].

3.4 Peak energy of localized energy level from valence band

The next defect parameter is E_{GA}, the peak energy of the acceptor-like localized states within the band gap of $BaSi_2$. This parameter was varied from 0.1 to 0.6 eV above the VBM. The obtained *J-V* curves are shown in Fig. 7(a). The values of J_{SC} slightly increased and the degradation can be attributed to a decrease in V_{OC}. This phenomenon can be explained as follows: when the defect level shifts from 0.1 to 0.6 eV from the VBM, band-to-defect transitions may occur, leading to degradation of the effective band gap in $BaSi_2$. Such degradation decreases the V_{OC}. These results suggest that the peak energy of localized states strongly affects the V_{OC}. In our case, the main difference between the ideal and measured p-$BaSi_2$/n-Si heterojunction solar cell is in the V_{OC}. Thereby, a value of E_{GA} = 0.4–0.5 eV is needed to reproduce the measured *J-V* curve.

3.5 Density of states of localized energy level

The last studied defect parameter is the DOS of acceptor-like localized energy level G_{GA} into the $BaSi_2$ film, which was varied from 1×10^{13} to 1×10^{20} cm^{-3} eV^{-1}. The simulated *J-V* curves are shown in Fig. 8(a). Figure 8(b) shows the J_{SC}, V_{OC}, *FF*, and η as a function of G_{GA}, extracted from the *J-V* curves. The values of J_{SC} and V_{OC} do not change when G_{GA} is below 1×10^{18} cm^{-3} eV^{-1}. As G_{GA} increases above 1×10^{18} cm^{-3} eV^{-1}, the presence of a localized energy level in the $BaSi_2$ film degrades the solar cell performance. Apparently, the effect of acceptor-like localized energy states with a Gaussian distribution is very similar to that of tail states. The reduction of J_{SC} can be reasonably understood by considering that the photogenerated carriers are trapped by the energy level. The degradation of the V_{OC} can be

explained by a decrease in J_{SC} and a possible increase of the dark saturated current density J_S of the heterojunction in the presence of defects in accordance with the relationship: $V_{OC}=k_BT/q$ ln (J_{SC}/J_S). Simultaneously, the presence of a barrier at the p-$BaSi_2$/n-Si interface results in a decrease of FF and η. In general, defect parameters of the localized energy level have a stronger influence on solar cell performance than band tail parameters.

3.6 Reproduction of the measured J-V curve

The defect effects of band tails and the localized energy levels in the $BaSi_2$ film led to comparable values between the simulation and measured results. A comparison of the J-V curves is shown in Fig. 9(a) with defect parameters values: $G_{TA}(G_{TD}) = 1.2 \times 10^{18}$ cm^{-3} eV^{-1}, $E_U = 0.10$ eV, $G_{GA} = 3.5 \times 10^{17}$ cm^{-3} eV^{-1}, $W_{GA} = 0.06$ eV, and $E_{GA} = 0.45$ eV, as plotted in Fig. 9(b). A good agreement was obtained between the simulation and measurements. We should note however that there is still a large divergence of curves in the current density range 20 to 33 mA/cm^2. Since the bending is very sensitive to model and physical processes responsible for the performance of solar cells, such divergence is a sign that either the model is too much simplified and additional parameters or processes should be considered or another set of numerical values should be used for those adjustable parameters. Thus, further studies are mandatory to reach a better fitting. Anyway, we confirmed that the defects are the main origin of the degradation of the p-$BaSi_2$/n-Si heterojunction solar cell performance. According to first-principle calculations based on the density-functional theory [51], B atoms occupy not only Si sites but also interstitial sites in $BaSi_2$, leading to the formation of deep localized states within the band gap of $BaSi_2$. Thereby the value of $E_{GA} = 0.45$ eV from the VBM is considered reasonable. The defect density of localized states N_T was calculated from G_{GA} and W_{GA} using Eq. (1) to be approximately 5×10^{16} cm^{-3}. Recently, supplying atomic H to $BaSi_2$ films has been found to effectively reduce the defects in undoped $BaSi_2$ films and markedly enhance the minority-carrier lifetime [56,57]. Thus, further studies on passivating $BaSi_2$ films

with atomic H might lead to higher η values.

4. Conclusion

In this paper, we used a numerical simulation, based on Silvaco ATLAS software, to model a p-$BaSi_2$/n-Si heterojunction solar cell and establish a reliable defect model to reproduce experimentally obtained *J-V* curve. Two band tails and one acceptor-like localized energy level were taken into consideration. We analyzed the effect of the Urbach tail energy, density of states of band tails, and density of the localized energy level in the band gap of $BaSi_2$. The peak energy and the standard deviation of the Gaussian distribution of the localized energy level had a considerable influence on V_{OC} and *FF,* respectively. Experimental *J-V* curves were well reproducible by simulations when the defect parameters were set as follows: a density of tail states $G_{TA}(G_{TD}) = 1.2 \times 10^{18}$ cm^{-3} eV^{-1}, a decay energy of the tail states $E_U = 0.10$ eV, a density of localized states $G_{GA} = 3.5 \times 10^{17}$ cm^{-3} eV^{-1}, a standard deviation of Gaussian distribution of the localized states $W_{GA} = 0.06$ eV, and a peak energy of the localized states $E_{GA} = 0.45$ eV.

Acknowledgements

The authors thank Professor H. Tadano for useful suggestions on Silvaco ATLAS software, Nanofabrication platform of the University of Tsukuba. This work was financially supported by the Japan Society for the Promotion of Science (JSPS) KAKENHI Grant Numbers 15H02237, 17K18865, and 18H03767.

Table 1 Input parameters for simulation [11].

Material	p-$BaSi_2$	n-Si
d [nm]	20	2×10^5
E_g [eV]	1.3[16,17]	1.1
n [cm^{-3}]	–	2×10^{15}
p [cm^{-3}]	2×10^{18}	–
Permittivity	14.0[46,48]	11.7
Affinity [eV]	3.2[44]	4.05
N_C [cm^{-3}]	2.6×10^{19}[46]	2.8×10^{19}
N_V [cm^{-3}]	2.0×10^{19}[46]	1.0×10^{19}
τ_e [μs]	8[20]	1.5
τ_h [μs]	8[47]	1.5
μ_e [cm^2/Vs]	500[45]	1000
μ_h [cm^2/Vs]	30[45]	500

Table 2 Parameters of the band tails and localized energy level.

	Band tails	Localized energy level
Urbach tail energy [eV]	0.10	–
Density of states [$cm^{-3}eV^{-1}$]	1.0×10^{16}	1.0×10^{15}
Peak energy from the VBM [eV]	–	0.37

Figure captions

Fig. 1. (a) Schematic diagram and defined mesh and (b) band alignment of the p-$BaSi_2$/n-Si heterojunction solar cell.

Fig. 2. Absorption coefficient of $BaSi_2$ and other solar cell materials [27,49,50].

Fig. 3. (a) *J-V* curves of simulated ideal and measured p-$BaSi_2$/n-Si heterojunction solar cell [34]. (b) Schematic of the band tails and the acceptor-like localized energy levels in $BaSi_2$ band gap.

Fig. 4. Simulated *J-V* curves as a function of Urbach tail energy E_U.

Fig. 5. (a) Simulated *J-V* curves as a function of G_{TA} (G_{TD}). G_{GA} was set to be 1×10^{15} cm^{-3} $eV^{-1}s$. (b) Solar cell parameters η, *FF*, V_{OC}, J_{SC} extracted from (a).

Fig. 6. (a) Simulated *J-V* curves as a function of E_U. G_{GA} was kept at 1×10^{15} cm^{-3} eV^{-1}. (b) Solar cell parameters *FF* and η against E_U, extracted from (a).

Fig. 7. (a) Simulated *J-V* curves as a function of peak energy of localized energy level E_{GA}. (b) Dependence of V_{OC} against on E_{GA}.

Fig. 8. (a) Simulated *J-V* curves as a function of density of states of localized energy level G_{GA}. (b) Solar cell parameters η, *FF*, V_{OC}, J_{SC} of p-$BaSi_2$/n-Si solar cells, extracted from (a).

Fig. 9. (a) Comparison of simulated and measured *J-V* characteristics of the p-$BaSi_2$/n-Si heterojunction solar cell. (b) Defect model in p-$BaSi_2$ used for simulation in (a).

Reference

[1] M. A. Green, Y. Hishikawa, E.D. Dunlop, D.H. Levi, J. Hohl-Ebinger, A.W.Y. Ho-Baillie, Solar cell efficiency tables (version 52), Prog. Photovolt: Res. Appl. 26 (2018) 427-436.

[2] W. S. Yang, B.-W. Park, E.H. Jung, N.J. Jeon, Y.C. Kim, D.U. Lee, S.S. Shin, J. Seo, E.K. Kim, J.H. Noh, S.I. Seok, Iodide management in formamidinium-lead-halide-based perovskite layers for efficient solar cells, Science 356 (2017) 1376.

[3] T. D. Lee, A.U. Ebong, A review of thin film solar cell technologies and challenges, Renew. Sust. Energ. Rev. 70 (2017) 1286-1297.

[4] T. K. Todorov, D.M. Bishop, Y.S. Lee, Materials perspectives for next-generation low-cost tandem solar cells, Sol. Energy Mater. Sol. Cells 180 (2018) 350-357.

[5] T. Matsui, H. Sai, K. Saito, M. Kondo, High-efficiency thin-film silicon solar cells with improved light-soaking stability, Prog. Photovoltaics 21 (2013) 1363-1369.

[6] J. Müller, B. Rech, J. Springer, M. Vanecek, TCO and light trapping in silicon thin film solar cells, Sol. Energy 77 (2004) 917-930.

[7] K. L. Chopra, P. D. Paulson, V. Dutta, Thin-film solar cells: an overview, Prog. Photovoltaics 12 (2004) 69-92.

[8] A. V. Shah, H. Schade, M. Vanecek, J. Meier, E. V. Sauvain, N. Wyrsch, U. Kroll, C. Droz, J. Bailat, Thin-film silicon solar cell technology, Prog. Photovoltaics 12 (2004) 113-142.

[9] A. Shah, P. Torres, R. Tscharner, N. Wyrsch, H. Keppner, Photovoltaic Technology: The Case for Thin-Film Solar Cells, Science 285 (1999) 692-698.

[10] C. Trompoukis, A. Abass, J-W Schüttauf, T. Bosserez, J. Rongè, J. Lauwaert, J. A. Martens, and R. Baets, Porous multi-junction thin-film silicon solar cells for scalable solar water splitting, Sol. Energy Mater. Sol. Cells182 (2018) 196-203.

[11] T. Suemasu, N. Usami, Exploring the potential of semiconducting $BaSi_2$ for thin-film solar cell applications, J. Phys. D: Appl. Phys. 50 (2017) 023001.

[12] J. Evers, G. Oehlinger, A. Weiss, Crystal Structure of Barium Disilicide at High Pressures, Angew. Chem. Int. Ed. Engl. 16 (1977) 659-660.

[13] Y. Inomata, T. Nakamura, T. Suemasu, F. Hasegawa, Epitaxial Growth of Semiconducting $BaSi_2$ Films on Si(111) Substrates by Molecular Beam Epitaxy, Jpn. J. Appl. Phys. 43 (2004) L478-L481.

[14] K. O. Hara, Y. Nakagawa, T. Suemasu, N. Usami, Realization of single-phase $BaSi_2$ films by vacuum evaporation with suitable optical properties and carrier lifetime for solar cell applications, Jpn. J. Appl. Phys. 54 (2015) 07JE02.

[15] S. Matsuno, R. Takabe, S. Yokoyama, K. Toko, M. Mesuda, H. Kuramochi, T. Suemasu, Significant photoresponsivity enhancement of polycrystalline $BaSi_2$ films formed on heated Si(111) substrates by sputtering, Appl. Phys. Express 11 (2018) 071401.

[16] K. Morita, Y. Inomata, T. Suemasu, Optical and electrical properties of semiconducting

$BaSi_2$ thin films on Si substrates grown by molecular beam epitaxy, Thin Solid Films 508 (2006) 363-366.
[17] K. Toh, T. Saito, T. Suemasu, Optical absorption properties of $BaSi_2$ epitaxial films grown on a transparent silicon-on-insulator substrate using molecular beam epitaxy, Jpn. J. Appl. Phys. 50 (2011) 068001.
[18] M. Kumar, N. Umezawa, M. Imai, $BaSi_2$ as a promising low-cost, earth-abundant material with large optical activity for thin-film solar cells: A hybrid density functional study, Appl. Phys. Express 7 (2014) 071203.
[19] S. W. Glunz, F. Feldmann, SiO_2 surface passivation layers – a key technology for silicon solar cells, Sol. Energy Mater. Sol. Cells 185 (2018) 260-269.
[20] K. O. Hara, N. Usami, K. Nakamura, R. Takabe, M. Baba, K. Toko, T. Suemasu, Determination of Bulk Minority-Carrier Lifetime in $BaSi_2$ Earth-Abundant Absorber Films by Utilizing a Drastic Enhancement of Carrier Lifetime by Post-Growth Annealing, Appl. Phys. Express 6 (2013) 112302.
[21] K. O. Hara, N. Usami, K. Toh, M. Baba, K. Toko, T. Suemasu, Investigation of the recombination mechanism of excess carriers in undoped $BaSi_2$ films on silicon, J. Appl. Phys. 112 (2012) 083108.
[22] M. Baba, K. Toh, K. Toko, N. Saito, N. Yoshizawa, K. Jiptner, T. Sekiguchi, K.O. Hara, N. Usami, T. Suemasu, Investigation of grain boundaries in $BaSi_2$ epitaxial films on Si(111) substrates using transmission electron microscopy and electron-beam-induced current technique, J. Cryst. Growth 348 (2012) 75-79.
[23] M. Baba, M. Kohyama, T. Suemasu, First-principles study of twin grain boundaries in epitaxial $BaSi_2$ on Si(111), J. Appl. Phys. 120 (2016) 085311.
[24] T. Suemasu, Exploring the possibility of semiconducting $BaSi_2$ for thin-film solar cell applications, Jpn. J. Appl. Phys. 54 (2015) 07JA01.
[25] A. Pokhrel, L. Samad, F. Meng, S. Jin, Synthesis and characterization of barium silicide ($BaSi_2$) nanowire arrays for potential solar applications, Nanoscale 7 (2015) 17450-17456.
[26] R. Vismara, O. Isabella, M. Zeman, Back-contacted $BaSi_2$ solar cells: an optical study, Opt. Express 25 (2017) A402-A408.
[27] R. Vismara, O. Isabella, M. Zeman, Organometallic halide perovskite/barium di-silicide thin-film double-junction solar cells, Proc. SPIE 9898 (2016) 98980J.
[28] M. Kobayashi, Y. Matsumoto, Y. Ichikawa, D. Tsukada, T. Suemasu, Control of Electron and Hole Concentrations in Semiconducting Silicide $BaSi_2$ with Impurities Grown by Molecular Beam Epitaxy, Appl. Phys. Express 1 (2008) 051403.
[29] M. Ajmal Khan, K.O. Hara, W. Du, M. Baba, K. Nakamura, M. Suzuno, K. Toko, N. Usami, T. Suemasu, In-situ heavily p-type doping of over 10^{20} cm^{-3} in semiconducting $BaSi_2$ thin films for solar cells applications, Appl. Phys. Lett. 102 (2013) 112107.

[30] Q. R. Deng, H. Chen, L. Chen, G. M. Wang, S. G. Wang, Y. L. Shen, Numerical simulation and optimization of Si/$BaSi_2$ heterojunction and $BaSi_2$ homojunction solar cells, J. Phys. D: Appl. Phys. 52 (2019) 075501.
[31] K. Kodama, R. Takabe, T. Deng, K. Toko, T. Suemasu, Spectroscopic evidence of photogenerated carrier separation by built-in electric field in Sb-doped n-$BaSi_2$/B-doped p-$BaSi_2$ homojunction diodes, Jpn. J. Appl. Phys. 57 (2018) 050310.
[32] K. Kodama, Y. Yamashita, K. Toko, T. Suemasu, Operation of $BaSi_2$ homojunction solar cells on p^+-Si(111) substrates and the effect of structure parameters on their performance, Appl. Phys. Express 12 (2019) 041005.
[33] D. Tsukahara, S. Yachi, H. Takeuchi, R. Takabe, W. Du, M. Baba, Y. Li, K. Toko, N. Usami, T. Suemasu, p-$BaSi_2$/n-Si heterojunction solar cells with conversion efficiency reaching 9.0%, Appl. Phys. Lett. 108 (2016) 152101.
[34] S. Yachi, R. Takabe, H. Takeuchi, K. Toko, T. Suemasu, Effect of amorphous Si capping layer on the hole transport properties of $BaSi_2$ and improved conversion efficiency approaching 10% in p-$BaSi_2$/n-Si solar cells, Appl. Phys. Lett. 109 (2016) 072103.
[35] T. Deng, T. Sato, Z. Xu, R. Takabe, S. Yachi, Y. Yamashita, K. Toko, T. Suemasu, p-$BaSi_2$/n-Si heterojunction solar cells on Si(001) with conversion efficiency approaching 10%: comparison with Si(111), Appl. Phys. Express 11 (2018) 062301.
[36] W. Shockley, H.J. Queisser, Detailed Balance Limit of Efficiency of p-n Junction Solar Cells, J. Appl. Phys. 32 (1961) 510.
[37] Y. Yamashita, T. Sato, K. Toko, T. Suemasu, Investigation of electrically active defects in undoped $BaSi_2$ light absorber layers using deep-level transient spectroscopy, Jpn. J. Appl. Phys. 57 (2018) 075801.
[38] T. Sato, C. Lombard, Y. Yamashita, Z. Xu, L. Benincasa, K. Toko, S. Gambarelli, T. Suemasu, Investigation of native defects in $BaSi_2$ epitaxial films by electron paramagnetic resonance, Appl. Phys. Express 12 (2019) 061005.
[39] Atlas User's Manual: Device Simulation Software from Silvaco International, Version 5.26.1.R, 10 April, 2018.
[40] M. Elbar, S. Tobbeche, A. Merazga, Effect of top-cell CGS thickness on the performance of CGS/CIGS tandem solar cell, Sol. Energy 122 (2015) 104-112.
[41] S. Michael, A.D. Bates, M.S. Green, Silvaco ATLAS as a solar cell modeling tool, in: 2005 31st IEEE Photovoltaic Specialists Conference 2005, pp. 719-721.
[42] S. Chala, N. Sengouga, F. Yakuphanoglu, Modeling the effect of defects on the performance of n-CdO/p-Si solar cell, Vacuum 120 (2015) 81-88.
[43] V. Gorge, A. Migan-Dubois, Z. Djebbour, K. Pantzas, S. Gautier, T. Moudakir, S. Suresh, A. Ougazzaden, Theoretical analysis of the influence of defect parameters on photovoltaic performances of composition graded InGaN solar cells, Mater. Sci. Eng. B 178 (2013) 142-148.

[44] T. Suemasu, K. Morita, M. Kobayashi, M. Saida, M. Sasaki, Band Diagrams of $BaSi_2$/Si Structure by Kelvin Probe and Current-Voltage Characteristics, Jpn. J. Appl. Phys. 45 (2006) L519-L521.
[45] T. Deng, T. Suemasu, D.A. Shohonov, I.S. Samusevich, A.B. Filonov, D.B. Migas, V.E. Borisenko, Transport properties of n- and p-type polycrystalline $BaSi_2$, Thin Solid Films 661 (2018) 7-15.
[46] D. B. Migas, V.L. Shaposhnikov, V.E. Borisenko, Isostructural $BaSi_2$, $BaGe_2$ and $SrGe_2$: electronic and optical properties, Phys. Status Solidi (b) 244 (2007) 2611-2618.
[47] M. Emha Bayu, Cham Thi Trinh, R. Takabe, S. Yachi, K. Toko, N. Usami, T. Suemasu, Minority-carrier lifetime and photoresponse properties of B-doped p-$BaSi_2$, a potential light absorption layer for solar cell, Jpn. J. Appl. Phys. 56 (2017) 05DB01.
[48] Nurul Amal Abdul Latiff, T. Yoneyama, T. Shibutami, K. Matsumaru, K. Toko, T. Suemasu, Fabrication and characterization of polycrystalline $BaSi_2$ by RF sputtering, Phys. Status Solidi (c) 10 (2013) 1759-1761.
[49] P. Löper, M. Stuckelberger, B. Niesen, J. Werner, M. Filipič, S.-J. Moon, J.-H. Yum, M. Topič, S. De Wolf, C. Ballif, Complex Refractive Index Spectra of $CH_3NH_3PbI_3$, Perovskite Thin Films Determined by Spectroscopic Ellipsometry and Spectrophotometry, J. Phys. Chem. Lett. 6 (2015) 66-71.
[50] P. D. Paulson, R.W. Birkmire, W.N. Shafarman, Optical characterization of $CuIn_{1-x}Ga_xSe_2$ alloy thin films by spectroscopic ellipsometry, J. Appl. Phys. 94 (2003) 879-888.
[51] D. Tsukahara, M. Baba, S. Honda, Y. Imai, K.O. Hara, N. Usami, K. Toko, J.H. Werner, T. Suemasu, Potential variations around grain boundaries in impurity-doped $BaSi_2$ epitaxial films evaluated by Kelvin probe force microscopy, J. Appl. Phys. 116 (2014) 123709.
[52] F. Urbach, The Long-Wavelength Edge of Photographic Sensitivity and of the Electronic Absorption of Solids, Phys. Rev. 92 (1953) 1324.
[53] W. Du, R. Takabe, S. Yachi, K. Toko, T. Suemasu, Enhanced spectral response of semiconducting $BaSi_2$ films by oxygen incorporation, Thin Solid Films 629 (2017) 17-21.
[54] M. Kumar, N. Umezawa, W. Zhou, M. Imai, Barium disilicide as a promising thin-film photovoltaic absorber: structural, electronic, and defect properties, J. Mater. Chem. A 5 (2017) 25293.
[55] O. Breitenstein, H. Straube, and K. Iwig, Lock-in thermography with depth resolution on silicon solar cells, Sol. Energy Mater. Sol. Cells 185 (2018) 66-74.
[56] Z. Xu, K. Gotoh, T. Deng, T. Sato, R. Takabe, K. Toko, N. Usami, T. Suemasu, Improving the photoresponse spectra of $BaSi_2$ layers by capping with hydrogenated amorphous Si layers prepared by radio-frequency hydrogen plasma, AIP Adv. 8 (2018) 055306.
[57] Z. Xu, D. A. Shohonov, A. B. Filonov, K. Gotoh, T. Deng, S. Honda, K. Toko, N. Usami,

D. B. Migas, V. E. Borisenko, T. Suemasu, Marked enhancement of the photoresponsivity and minority-carrier lifetime of $BaSi_2$ passivated with atomic hydrogen, Phys. Rev. Mater. 3 (2019) 065403.

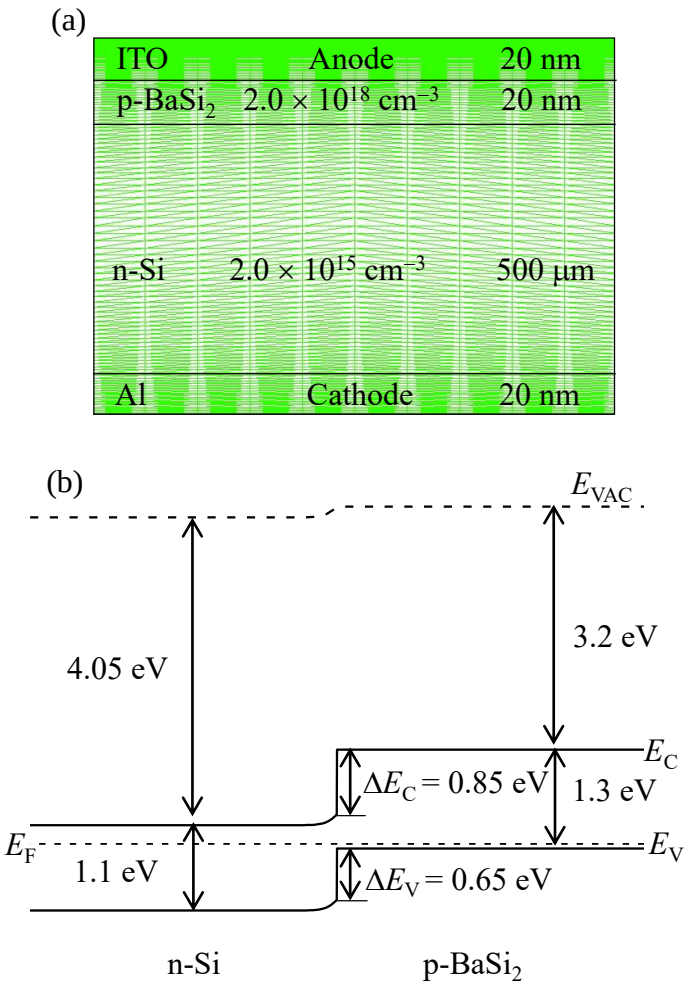
(a)
ITO
Anode
20 nm
p-BaSi2
2.0 × 10^18 cm^−3
20 nm
n-Si
2.0 × 10^15 cm^−3
500 μm
Al
Cathode
20 nm
(b)
E_VAC
4.05 eV
3.2 eV
E_C
ΔE_C = 0.85 eV
1.3 eV
E_F
1.1 eV
E_V
ΔE_V = 0.65 eV
n-Si
p-BaSi2

Fig. 1

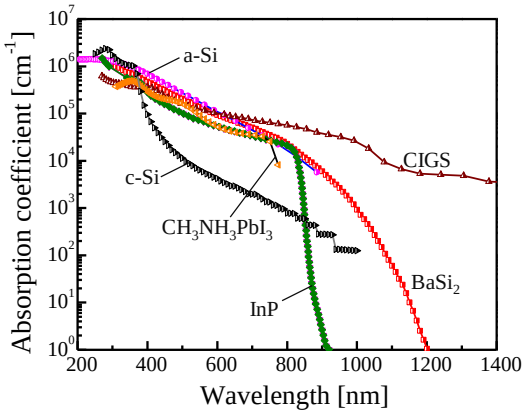
Absorption coefficient [cm^{-1}]
Wavelength [nm]
a-Si
c-Si
$CH_3NH_3PbI_3$
CIGS
$BaSi_2$
InP

Fig. 2

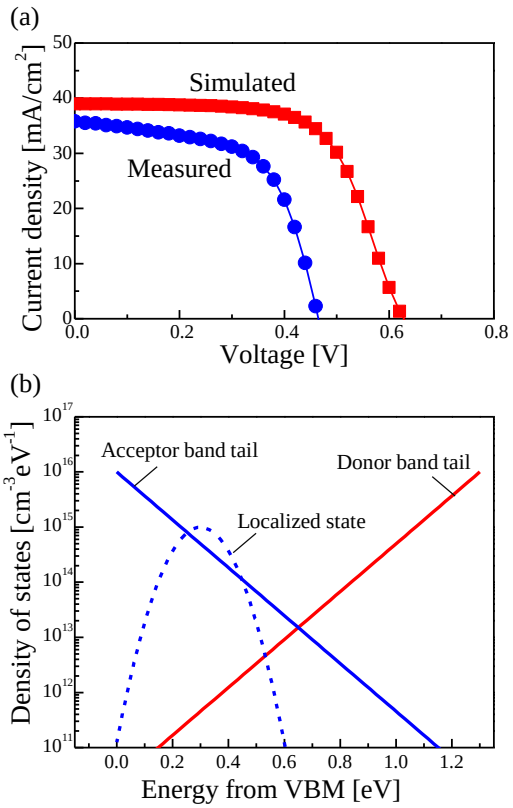
(a)
Current density [mA/cm^2]
Simulated
Measured
Voltage [V]
(b)
Density of states [cm^{-3}eV^{-1}]
Acceptor band tail
Donor band tail
Localized state
Energy from VBM [eV]

Fig. 3

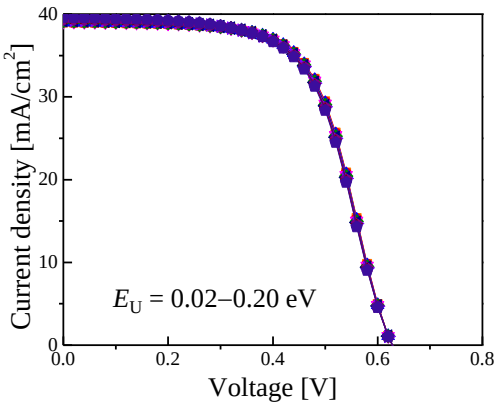
Current density [mA/cm^2]
Voltage [V]
E_U = 0.02–0.20 eV
0
10
20
30
40
0.0
0.2
0.4
0.6
0.8

Fig. 4

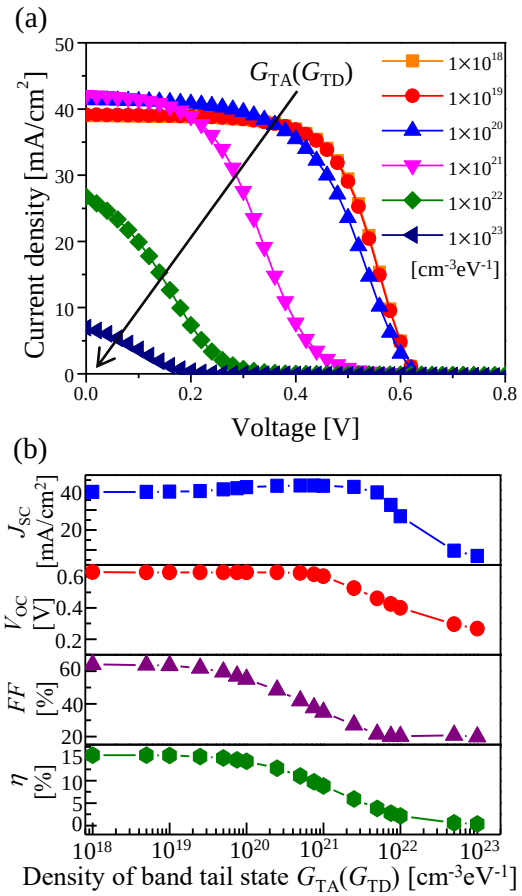
(a)
Current density [mA/cm^2]
Voltage [V]
$G_{TA}(G_{TD})$
1×10^{18}
1×10^{19}
1×10^{20}
1×10^{21}
1×10^{22}
1×10^{23}
[cm^{-3}eV^{-1}]
(b)
J_{SC} [mA/cm^2]
V_{OC} [V]
FF [%]
η [%]
Density of band tail state $G_{TA}(G_{TD})$ [cm^{-3}eV^{-1}]

Fig. 5

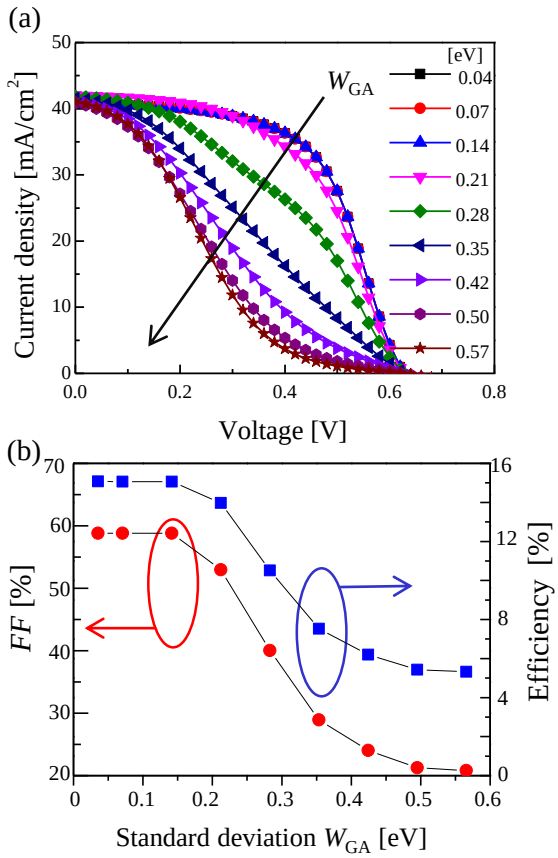
(a)
Current density [mA/cm^2]
Voltage [V]
W_{GA}
[eV]
0.04
0.07
0.14
0.21
0.28
0.35
0.42
0.50
0.57
(b)
FF [%]
Efficiency [%]
Standard deviation W_{GA} [eV]

Fig. 6

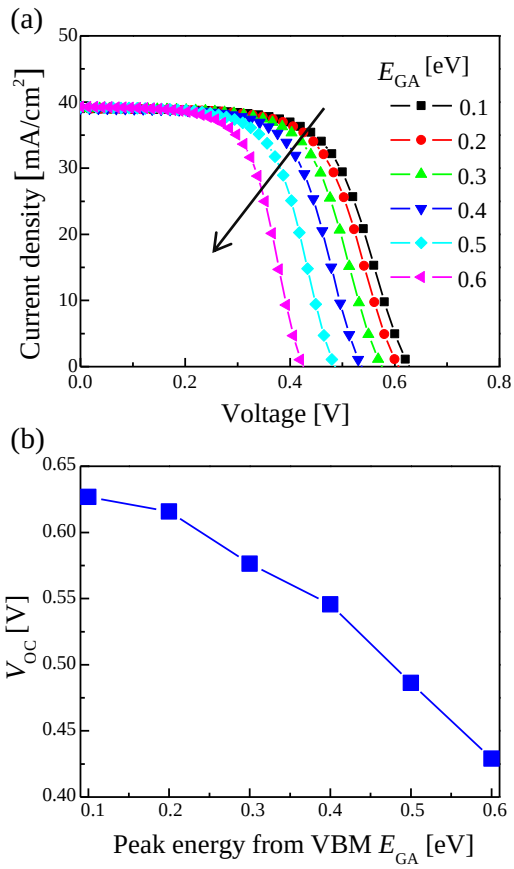
(a)
Current density [mA/cm^2]
Voltage [V]
E_{GA} [eV]
0.1
0.2
0.3
0.4
0.5
0.6
(b)
V_{OC} [V]
Peak energy from VBM E_{GA} [eV]

Fig. 7

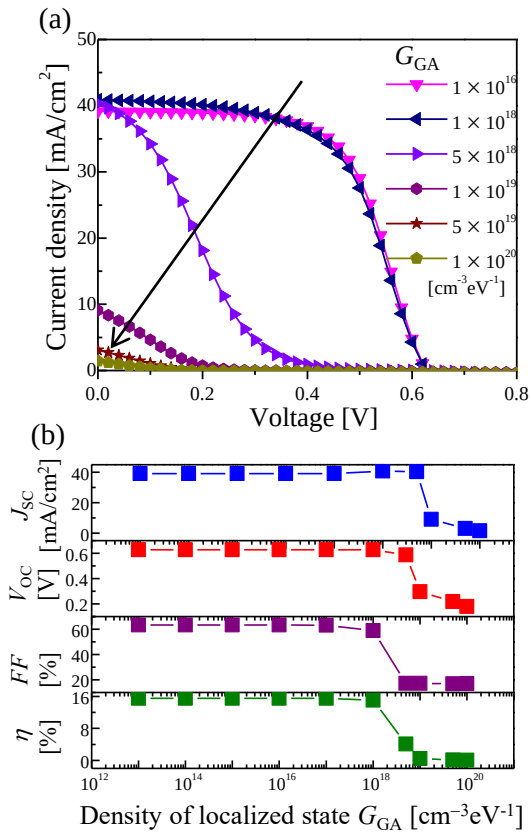
(a)
Current density [mA/cm^2]
Voltage [V]
G_{GA}
1 × 10^{16}
1 × 10^{18}
5 × 10^{18}
1 × 10^{19}
5 × 10^{19}
1 × 10^{20}
[cm^{-3}eV^{-1}]
(b)
J_{SC} [mA/cm^2]
V_{OC} [V]
FF [%]
η [%]
Density of localized state G_{GA} [cm^{-3}eV^{-1}]

Fig. 8

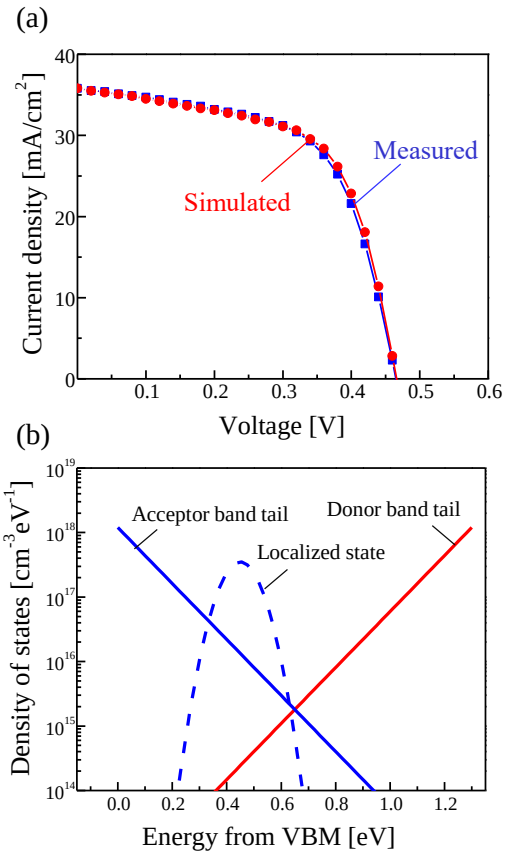
(a)
Current density [mA/cm^2]
Voltage [V]
Measured
Simulated
(b)
Density of states [cm^{-3}eV^{-1}]
Energy from VBM [eV]
Acceptor band tail
Donor band tail
Localized state

Fig. 9